IJE TRANSACTIONS A: Basics Vol. 37 No. 07, (July 2024) 1357-1368

International Journal of Engineering

Journal Homepage: www.ije.ir

Design and Optimization of the Dual-Stator Axial-Field Flux-Switching Permanent Magnet Motor with High-Torque Density and Low-cost

F. Farrokh*[a], A. Vahedi[b], H. Torkaman[c], M. Banejad[a]

[a] *Faculty of Electrical Engineering, Shahrood University of Technology, Shahrood, Iran*
[b] *Department of Electrical Engineering of Iran University of Science & Technology, Tehran, Iran*
[c] *Faculty of Electrical Engineering, Shahid Beheshti University, Tehran, Iran*

PAPER INFO

Paper history:
Received 27November 2023
Received in revised form 06 January 2024
Accepted 10 January 2024

Keywords:
Dual-Stator Axial Field Flux-Switching Machine
High-Torque Density
High-efficiency
Low-cost
Thermal Stress
Electric Vehicles

ABSTRACT

In this paper, a new dual-stator axial field flux-switching permanent magnet (DSAFFSPM) motor has been proposed to improve the torque density and cost of the machine. In this topology, the 12-pole dual-stator has been located on both sides of one 10-pole inner-toothed rotor. The dual-stator has hosted permanent magnet (PM) type of Bar-PM and the coils. The novelty of this study is development of a technique that can be implemented on PM of the DSAFFSPM structure. In this regard, the proposed analytical design with a sizing equation has been presented and multi-objective optimization is employed to achieve the optimum size by Multi-Objective Genetic Algorithm (MOGA) method. The machine characteristics are acquired and analyzed utilizing the 3D finite element method (3D-FEM). A comparative study has been done to prove the superiority of the performance indices. This topology demonstrates the high-power density and the low vibration and noise due to lower torque ripple and cogging torque. Meanwhile, the Bar-PM topology has lower core loss and thermal stress due to high-efficiency. Consequently, the proposed model provides high torque density and low cost, specifically designed for electric vehicle (EVs) applications.

***doi**: 10.5829/ije.2024.37.07a.14*

Graphical Abstract

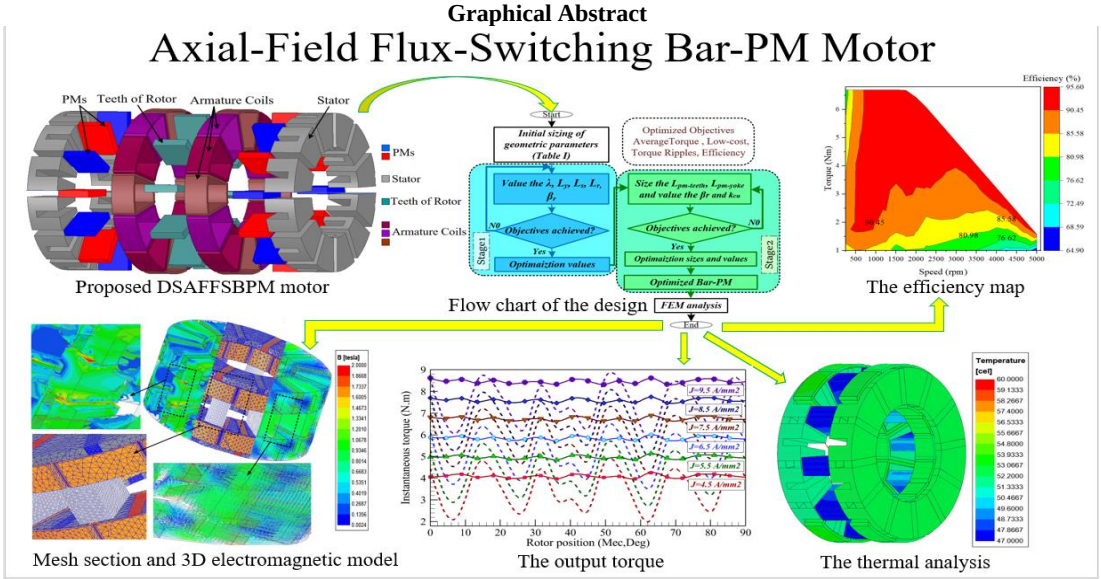

*Corresponding Author Email: F.farrokh94@yahoo.com (F. Farrokh)

Please cite this article as: Farrokh F, Vahedi A, Torkaman H, Banejad M. Design and Optimization of the Dual-Stator Axial-Field Flux-Switching Permanent Magnet Motor with High-Torque Density and Low-cost. International Journal of Engineering, Transactions A: Basics. 2024;37(07):1357-68.

1. INTRODUCTION

Different types of technology machines include axial and radial flux machines. Studies showed that axial flux machines (AFPM) have higher torque and power density (1-3), as well as efficiency (4-6). Axial field flux-switching machines (AFFSPM) have limited torque density due to the location of PMs and coils, but still have higher torque and efficiency than radial flux machines and can reduce costs. New motor designs have been proposed in recent publications (7-10). One used non-rare-earth PM for high-torque density (11). While another achieves even higher torque density with rotor-excited PM (12). The AFFSPM design with E-core reduces cost and PM volume, but also has lower average torque compared to U-core and C-core designs (13). Kim et al. (14), AFFSPM have presented with a rotor middle and external dual-stator. Topologies try to maintain a phase shift of $\pm\pi$ electric radians, topology 1 (shifting stator 2) has the highest output torque compared to topology 2 (shifting rotor poles of stator 2) and topology 3 (shifting both stator 2 and rotor poles of stator 2).

Newly, three conventional DSAFFSPM structures with internal dual-rotor, internal single teeth rotor (ISTR), and external dual-rotor have been compared together for EV application. The findings show that, the internal single-rotor topology is a suitable candidate for EV application because it has high efficiency, and high torque density (15). Nevertheless, it has troubled higher cogging torque and torque ripple.

Own to reduction the reserve of rare-earth PM materials (such as Ndfe35) and market monopoly have affected price fluctuation for further application of PM motors in EVs. Some researchers suggested non-rare-earth PM (such as ferrite) types (11). The results showed that compared with rare-earth PM materials have low performance. To further make it better torque density a type of hybrid excitation (both DC and AC windings) machine has been proposed (16-19). However, this leads to low torque, power densities, provision of the field excitation source, an increase in cost, and loss. Reducing the consumption of rare-earth PMs compromises the AFFSPM motor performance because the main flux structure is supplied by PM. For this reason, has made the issue of PM reduction less attention by researchers. Recently, reducing the consumption of rare-earth PMs and cost material has become a hot topic, particularly in PM machines (20-22).

The main objective of present work is to design a dual-stator axial-field flux-switching Bar-PM (DSAFFSBPM) motor with high-torque density and low-cost for EV application. Employing a technique that is aimed at the reducing value of rare-earth PM in the DSAFFSBPM, so that it can be implemented on the conventional ISTR-DSAFFSPM structure. The main contribution novelties of this paper are a novel technique that has been implemented on PMs for the first time. Then, the technique aims to achieve multi-objective optimization, which involves reducing the increase in torque density, lowering costs, and decreasing thermal temperature using air channels. The challenges addressed by this paper are:

1) To be provided the high-torque density and the low-cost simultaneously.
2) Due to their doubly salient structure, the cogging torque is an unfavourable effect.
3) Due to their high air-gap flux density caused by flux focusing effects be suffered torque ripple.

2. THE STRUCTURE AND OPERATION PRINCIPLE

2. 1. Proposed New Structure Figure 1 shows the 3D exploded model. The configuration of the conventional ISTR-DSAFFSPM motor is illustrated in Figure 1. The DSAFFSBPM motor is also presented in Figure 1.b. In this structure, unlike the former types of AFPMs, no magnet exists in the rotor. Therefore, the stator hosted Bar-PM and coils. The only difference is that one slot comprises segments of rare-earth magnets as Bar-PM, which are circumferentially magnetized, and embedded precisely in the stator yoke and stator teeth of these slots, and tightened. The stator is created of 12 poles on each side. 12 concentric-coils twist the poles in two 3-phase complies alternately. The rotor of this topology is of toothed type.

2. 2. The Operation Principle To demonstrate the operational principles of this structure, a 2D model is proposed as shown in Figure 2. It illustrates four rotor positions for PM flux. These four special positions rotor a, b, c, and d comply with the four points of maximum

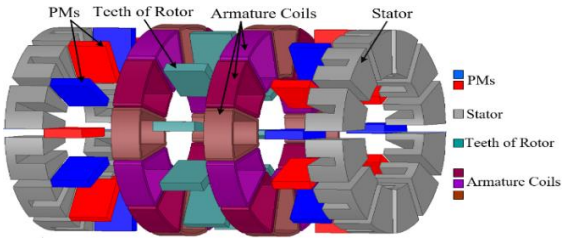

(a) Conventional ISTR-DSAFSPM motor

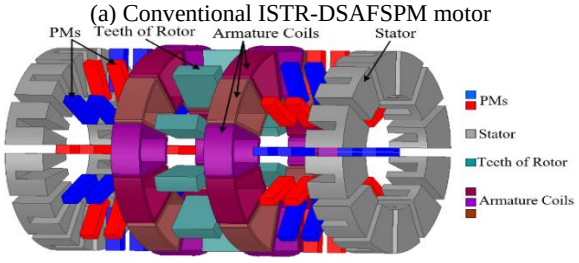

(b) Proposed DSAFFSBPM motor

Figure 1. The 3D exploded view

positive, zero, maximum negative, and zero flux of phase A, respectively. Figure 2(a); the rotor tooth T2 is placed almost in front of the stator tooth, which the winding A1 wraps. The magnetic direction of the PM is to the right, as a result, the direction of the magnetic flux is upward in winding A1. The magnetic flux passes the rotor tooth T1 and the air-gap, which enters the stator tooth S1. The flux-linkage A1 is positive maximum; this is dubbed the positive position. When the rotor rotates θ_r=*9º* Mec in Figure 2(b), the rotor tooth T2 and the PM are aligned, so the flux in the winding becomes zero. This position is dubbed the zero position of the rotor. When the rotor rotates another at θ_r=*9º* Mec in Figure 2(c), the rotor tooth T2 is almost in front of the stator tooth S2. The flux-linkage A1 is negative maximum; this is dubbed the negative position. In Figure 2(d), As the rotor rotates at θ_r=*27º* Mec, the rotor tooth T2 is located in front of the slot; it means, it is placed in the second zero position; this process repeats to generate the periodic flux-linkage, and the back-EMF.

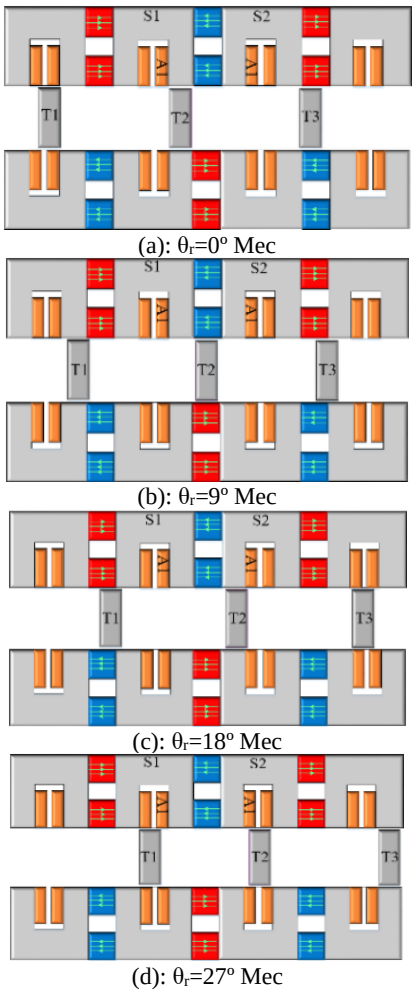

(a): θr=0º Mec

(b): θr=9º Mec

(c): θr=18º Mec

(d): θr=27º Mec

Figure 2. Four specific positions rotor of the 3-phase DSAFFSBPM motor

Inferred to Equation 1, when a sinusoidal current has followed the equations, can result in the back-EMF voltage is formed, hence electromagnetic torque was generated.

$$I_a = I_{max}\sin(\theta)$$
$$E_a = E_{max}\sin(\theta) \quad \text{(1-a)}$$

$$I_b = I_{max}\sin(\theta - 2\pi/3)$$
$$E_b = E_{max}\sin(\theta - 2\pi/3) \quad \text{(1-b)}$$

$$I_c = I_{max}\sin(\theta + 2\pi/3)$$
$$E_c = E_{max}\sin(\theta + 2\pi/3) \quad \text{(1-b)}$$

3. DESIGN PROCEDURE AND MULTI-OBJECTIVE OPTIMIZATION

3. 1. The Sizing Equations of DSAFFSBPM Motor

The output power equation of the motor for EVs, and the dimensions of the motor is deduced according to Farrokh et al. (15), the output power of the DSAFFSBPM motor be expressed as follows:

$$P_{0ut} = \frac{m}{T}\int_0^T e(t).i(t)\,dt \quad (2)$$

According to the current and the phase PM flux-linkage are sinusoidal, the output power writes as follows:

$$P_{0ut} = \frac{m}{T}\int_0^T E_m \sin(\frac{2\pi}{T}t)\, I_m \sin(\frac{2\pi}{T}t)\,dt \quad (3)$$

$$P_{0ut} = \frac{m}{2} E_m I_m \quad (4)$$

In which E_m is maximum voltage, and I_m is the current magnitude. The output power is derived by adding the motor efficiency is η as stated below:

$$P_{0ut} = \frac{m}{2} E_m I_m \eta \quad (5)$$

According to Equation 1, the EMF in the coils (e), when the armature is open-circuit and only the flux PM exists, is given as follows:

$$\mathrm{e} = -\frac{d\psi_m}{dt} = -N_{ph}\frac{d\varphi}{d\theta}\frac{d\theta}{dt} = -N_{ph}\frac{d\varphi}{d\theta}\omega_r \quad (6)$$

where Ψ_m term is the flux linkage of the phase. The term N_{ph} is the number of the winding turns per phase, φ_m term will be the flux-linkage of one turn, θ and ω_r are the rotor position and the angular speed of rotor, respectively. According to Equation 1, the flux-linkage is expressed as follows:

$$\varphi_m = \varphi_R \cos(P_r\theta) \quad (7)$$

where φ_R and P_r are the flux magnitude and the number of the rotor poles, respectively.

Substituting the Equation 7 into Equation 6, the back-EMF, yields as follows:

$$e = N_{ph}\ \omega_r P_r \varphi_R \sin(P_r\theta) = E_m \sin(P_r\theta) \quad (8)$$

According to Figure 2(a), this position is the maximum flux passing, therefor the air-gap area (A_g) placed between the stator tooth and the rotor pole is inferred as stated as follows:

$$A_g = \beta_r \times \frac{(D_{so}-D_{Si})}{2} \quad (9)$$

where β_r is the pole pitch which is shown in Figure 3. D_{so} and D_{si} are the outer and inner diameters of the DSAFFSB-PM motor, respectively. τ_s is stator pole pitch. The average diameter of air-gap is given below:

$$\tau_s = \frac{\pi\, D_{so}}{P_s} \quad (10)$$

$$\beta_r = \beta_{st} + \beta_{pm} + \beta_t = \frac{\tau_s}{4} \quad (11)$$

where P_s is the number of the stator poles. By inserting Equations 10, and 11 into Equation 9, it can be determined as:

$$A_g = \frac{\pi\,(D_{so}^2-D_{si}^2)}{8\,P_s} \quad (12)$$

From Equation 13, the flux magnitude is calculated as:

$$\varphi_R = K_l\, K_g\ B_{gmax}\, \beta_i\, \frac{\pi}{8\,P_s}\,(D_{so}^2 - D_{si}^2) \quad (13)$$

In which K_l is a leakage flux factor and K_g is the factor of the air-gap flux density distribution. B_{gmax} is the peak value of the air-gap flux density in the no-load mode. β_i is the area ratio of the stator tooth and stator tooth-slot unit. Substituting Equation 13 into Equation 8, E_m will be stated as follows:

$$E_m = N_{ph}\ \omega_r P_r K_l\, K_g\ B_{gmax}\, \beta_i\, \frac{\pi}{8\,P_s}\,(D_{so}^2 - D_{si}^2) \quad (14)$$

Due to the concentration of the maximum electrical load in the smallest radius of axial-flux machines, the limit of this parameter is considered in the inner radius of the machine. Therefore, the electrical loading, denoted as A_s, is highest at this point. A_s is given below:

$$A_s = 2m\, N_{ph}\, \frac{I_{rms}}{\pi\, D_{si}} \quad (15)$$

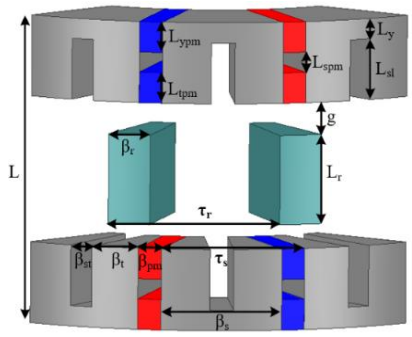

Figure 3. Design Parameters of the DSAFFSBPM

The maximum of sinusoidal current is given as:

$$I_m = \sqrt{2}\, I_{rms} = \frac{\sqrt{2}}{2}\, \frac{\pi\, A_s D_{si}}{m\, N_{ph}} \quad (16)$$

By converting the rotor speed to rpm infer to $\omega_r = 2\pi n_r/60$ and by Substituting Equations 14 and 16 into Equation 5 yields:

$$P_{0ut} = \frac{\sqrt{2}\pi^3}{480}\, \frac{P_r}{P_s}\, K_l\, K_g\, \lambda(1-\lambda^2)\, A_s\, B_{gmax}\, \beta_i\, D_{so}^3 n_r\, \eta \quad (17)$$

where λ is the ratio of the inner and outer stator diameters. A_s is the maximum current density and n_r is the speed of the rotor.

The output torque is calculated as follows:

$$T_{0ut} = \frac{3\pi^2\sqrt{2}}{48}\, \frac{P_r}{P_s}\, K_l\, K_g\, \lambda(1-\lambda^2)\, A_s\, B_{gmax}\, \beta_i D_{so}^3 \eta \quad (18)$$

A fixed outer diameter of the stator is a design limiting factor in an electrical vehicle, which impacts machine performance. Therefore, adopting the value optimal λ lead to the best electrical and magnetic loading. The λ as the objective function from the torque equation estimated as follows:

$$T_{0ut}(\lambda) = \lambda - \lambda^3 \quad (19)$$

$$\lambda_{max} = \frac{1}{\sqrt{3}} = 0.57 \quad (20)$$

Equation 21 is applied in opting for the internal diameter thus, maximize the average output torque. According to Zhao et al. (17), the outer diameter of the stator can be expressed as follows:

$$D_{so} = \sqrt[3]{\frac{480\, P_{out}\, P_s}{\sqrt{2}\,\pi^3\, P_r\, K_l\, K_g\, \lambda(1-\lambda^2)\, A_s\, B_{gmax}\, \beta_i\, n_r \eta}} \quad (21)$$

The primary dimensions of the designed motors are listed in Table 1 and illustrated in Figure 3.

TABLE 1. Primary parameters of investigated DSAFFSPM motor

Parameter	Symbol	Proposed Bar-PM	Optimized Bar-PM
Nominal power (kW)	P_n	1	
Rated speed (rpm)	n_r	1500	
Rated current (A/mm^2)	J	7.5	
No, of phase	m	3	
Slots / rotor poles	P_s / P_r	12/10	
Stator outer diameter (mm)	D_{so}	140	
Axial length (mm)	L	64	
Air gap length (mm)	g	1	
Stator pole pitch (deg)	$_s\beta$	30	
Rotor pole pitch (deg)	β_r	12.5	15.5

PM pitch (deg)	$_{pm}\beta$	6	
Rotor yoke with (mm)	L_y	5	4.5
Teeth magnet length (mm)	L_{tpm}	7.5	6
Yoke magnet length (mm)	L_{ypm}		7
Machine volume (L)	-	0.98	

3. 2. Multi-Objective Optimization There are many multi-objective algorithms, some struggle to balance solution quality and diversity. However, the MOGA adjusts this balance by combining domain structure and evolutionary operation. MOGA considers both the quality and diversity of optimal solutions during optimization and has been applied successfully in various fields, including transportation (23-25). The MOGA be is utilized to optimize the electromagnetic performance of the DSAFFBPM motor based on objective function (OF). The GA adopts initial design parameters of the rotor, stator as well as PMs such as λ, L_y, L_s, L_r, $L_{pm-teeth}$, $L_{pm-yoke}$, and β_r to comprehensive analysis; when all design objectives are simultaneously and multi-dimensionally. Optimized objectives such as average torque (T_{av}), low-cost ($cost$), torque ripples (T_{ri}), and efficiency follow to find out a convergent response as follows.

$$\begin{cases} Objective\ function: \\ \max(T_{av}, \eta)\ and\ min(cost, T_{ri}) \end{cases} \quad (22)$$

$$\begin{cases} Constraint: \\ T_{av} \geq 5.87N.m, \eta \geq 92.96\% \\ cost \leq \$60, T_{ri} \leq 45.31\% \end{cases} \quad (23)$$

$$\begin{cases} Variable\ stage1 = [\lambda, \beta_r, L_y, L_s, L_r] \\ Boundry\ condition\ stage1: \\ 0.55 \leq \lambda \leq 0.57, 6.28 \leq \beta_r \leq 10.46\ deg \\ 4.5 \leq L_y \leq 6.5\ mm, 20 \leq L_s \leq 21\ mm \\ 20 \leq L_r \leq 22\ mm \\ Variable\ stage2 = [\beta_r, L_{ypm}, L_{tpm}, k_{cu}] \\ Boundry\ condition\ stage2: \\ 10.46 \leq \beta_r \leq 15.5\ deg, 7 \leq L_{ypm}, L_{tpm} \leq 8\ mm \\ 0.68 \leq k_{cu} \leq 0.7 \end{cases} \quad (24)$$

The GAO employs a multi-objective function to optimize its design. Eight design parameters can affect the performance of the genetic algorithm, as outlined by Equation 24 and Figure 4. As shown in Figure 5, after approximately 40 generations of genetic optimization, the two stages converge to the optimal solution. The GAO then optimizes eight key parameters to achieve four optimized objectives, resulting in improved performance. These parameters and associated performance improvements are listed in Table 2.

The design procedure of the DSAFFSBPM motor is illustrated in the form of a flowchart as shown in Figure 4. The parameters are purposefully optimized in two stages, which can provide an accurate response in a minimum time. In stage 1, multi-dimensional optimization is done with the parameters denoted and without reducing the PM value such as λ, L_y, L_s, L_r, $L_{pm-teeth}$, $L_{pm-yoke}$, and β_r are optimized. In stage 2, two affecting parameters βr and slot fill factor (k_{cu}) are applied to optimize by reducing the PM value. The derivative results of MOGA have been visible in the optimized model as shown in Figure 5, which are marked with green bubble points.

In Equation 23, the variables T_{av}, η, and T_{ri} are analyzed using the conventional ISTR model. The $cost$ of optimizing and reducing PMs is found to be lower when using the conventional ISTR model than the proposed Bar-PM model. In Equation 24, the parameters are limited in stage 1 based on the conventional ISTR model, and then in stage 2, they are restricted based on the considered cost.

The effect of MOGA on electromagnetic performance and both initial and optimized parameters are discussed. For investigation and comparison, both initial and optimized performances are recorded in Table 2. Based on electromagnetic performances, the analysis represents that T_{av} is improved by as much as 5.14%, decreased T_{ri} as much as 70.44% enhanced η by 6.37%, and reduced cost by10.52%. As well as, based on MOGA, initial and optimized design parameters received are registered, in Table 1. The final optimized model is investigated further in the following sections.

4. FEM ANALYSIS RESULTS AND ELECTROMAGNETIC PERFORMANCE

After the design of the optimized structural model, the electromagnetic performance of the motors is assessed using 3D-FEM and numerical analysis.

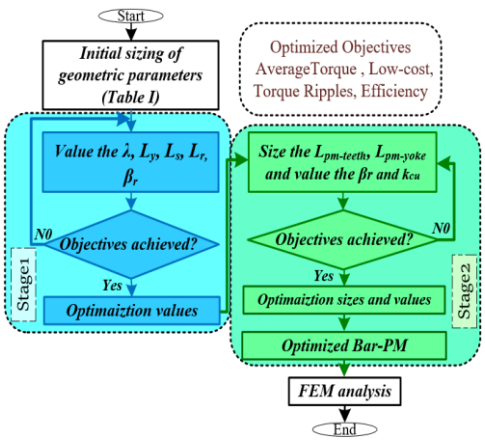

Figure 4. Flow chart of the design procedure for DSAFFSBPM motor

TABLE 2. Electromagnetic performance analysis of and optimized models

Model, Parameter	Initial design Bar-PM	Optimized design Bar-PM
T_{av} [Nm]	6.41	6.74
T_{ri} [%]	14.04	4.15
Cost [$]	62.51	55.98
η [%]	94.13	94.19

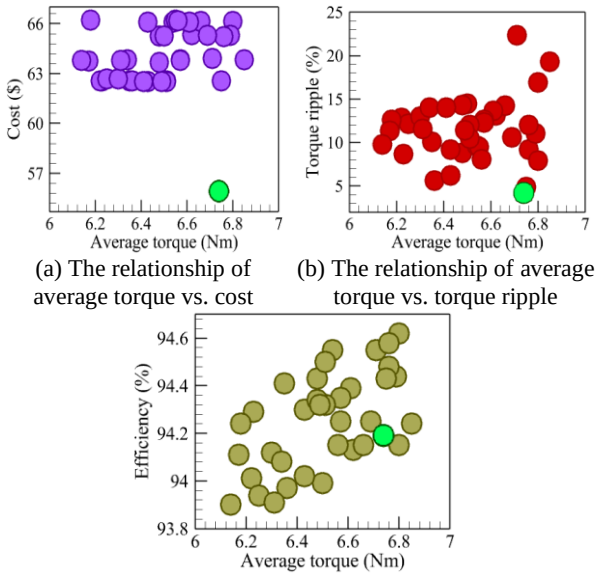

(a) The relationship of average torque vs. cost

(b) The relationship of average torque vs. torque ripple

(c) The relationship of average torque vs. efficiency

Figure 5. The optimization results of the four optimization objectives

4. 1. Investigation on Open-Circuit Magnetic Field Distribution When the stator windings are in open-circuit status, the open-circuit field distribution is only performed through the Bar-PMs. Rotor rotation against 3-phase winding leads to the polarity of the flux and flux focusing. Finally, the concept of "switching flux" is employed in the motor. The $\theta_r=9^o$ Mec and $\theta_r=27^o$ Mec shown in Figures 6(a) and 6(c) address the status when the rotor teeth are located in the front of the stator teeth. In this status, the maximum flux linkage with the coil takes place respectively in negative and positive values with a magnetic field density of roughly 1.33T for the proposed Bar-PM model. Figure 6(b) illustrate $\theta_r=18^o$ Mec rotor position in which the coils 'linkage flux achieves zero. The maximum flux density is for the optimized Bar-PM model that did not exceed 1.1T in the worst-case scenario. The concentration of flux is higher in the stator yoke than in the stator teeth. As a result, the length of the PM on the side of the stator yoke is slightly longer than the PM on the side of the stator teeth. This ensures proper distribution of flux in these areas. The maximum flux concentration in the PMs in three different rotor modes did not exceed 1.06 T.

4. 2. Analysis of the Flux Linkage and Induced Voltage Characteristics According to Equation 7, Figure 7, depicts the three-phase open-circuit flux-linkage in the DSAFFSPM models. The maximum flux-linkage amplitude is 0.047 Wb for the optimized Bar-PM model; then, the proposed Bar-PM model is 0.048 Wb. A 2.08% decrease linkage-flux in the optimized Bar-PM model compared to proposed Bar-PM model is due alter in slots. Figure 7 specifies where the phase difference of $2\pi/3$ of the electrical degree of 3-phase flux-linkage sinusoidal waveform. Therefore, confirms the operation of DSAFFSPM as an AC brushless machine.

In Figure 8, 3-phase induced back-EMF sinusoidally in open-circuit voltage is compared for the DSAFFSPM models at @1500 rotor speed. The back-EMF amplitudes of the proposed and optimized Bar-PM models are 77.57, and 73.89 V, respectively. According to Equations 7 and 8, it is expected that the amplitude of flux-linkage is less than 2.08% in the optimized Bar-PM model. Consequently, its amplitude of the induced voltage range is reduced by 4.74%.

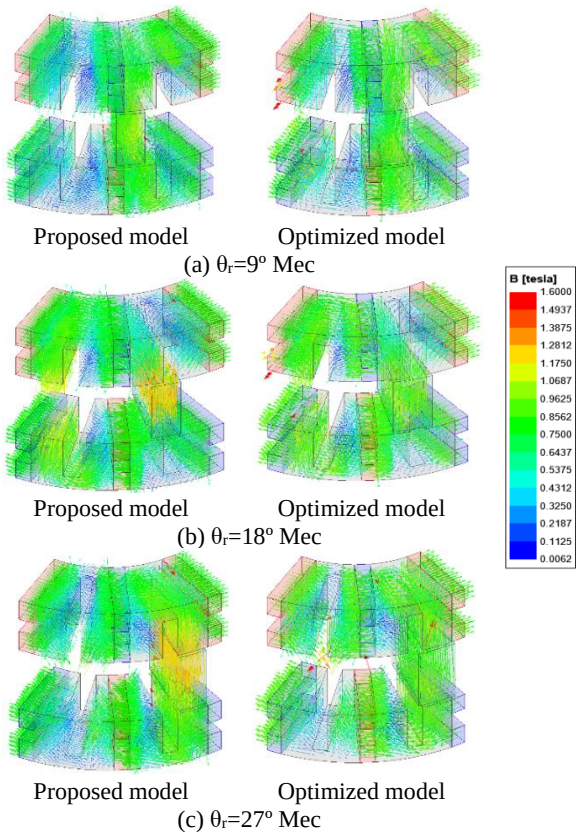

(a) $\theta_r=9^o$ Mec

(b) $\theta_r=18^o$ Mec

(c) $\theta_r=27^o$ Mec

Figure 6. The 3D open-circuit magnetic field distribution in three fundamental rotor positions of Bar-PM models

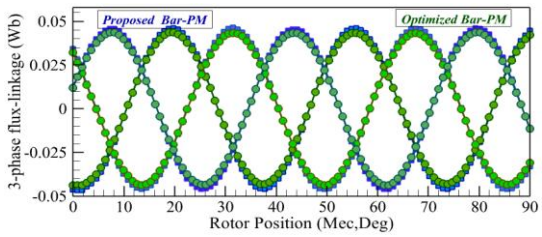

Figure 7. The flux-linkage sinusoidal waveform in the 3-phase DSAFFSPM motor

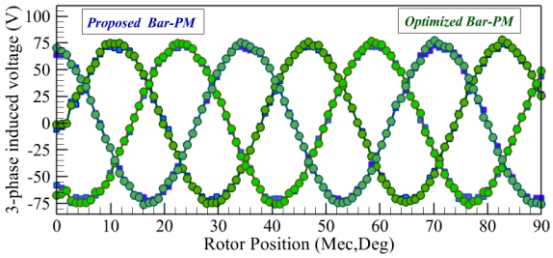

Figure 8. The back-EMF in the 3-phase DSAFFSM-B motor

4. 3. The Induced Voltage Harmonic Spectrum

The λ parameter and the magnet's thickness must be adopted at a low-cost with promising harmonics spectrum. By considering λ=*0.57*, β_r increases amount of 24% and L_{pm} decreases 25% in the magnetization direction, the improvable voltage harmonics spectrum has opted for a low-cost. Based on the normalized domain values of the harmonic spectrum of the three presented models are manifested in Figure 9. The harmonic spectrum of the voltage is improved compared to the conventional ISTR. The harmonic order 5 of the conventional ISTR model equals 5%, while the harmonic order value is 1.2% for the proposed model. The optimized Bar-PM model is equal to 1.1%, which has decreased by 8.33%. The harmonic order 7 of the conventional ISTR model equals 2.7%. Meanwhile, the proposed and optimized model's harmonic order value is under 1%. From the sight of the harmonics spectrum, the proposed motor has an acceptable condition.

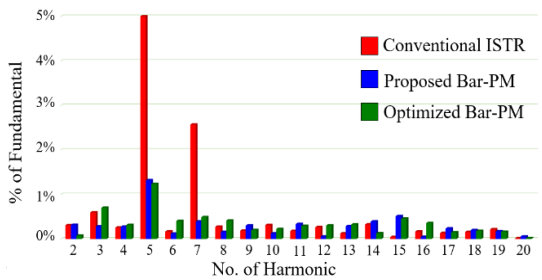

Figure 9. The harmonic spectrum of the back-EMF based on the normalized domain of the harmonics

4. 4. The Cogging Torque and Output Torque Analysis

In Figure 10, the DSAFFSPM models compare the cogging torque and output torque. The conventional ISTR and proposed Bar-PM have peak-to-peak cogging torque values of 2.52 N.m and 1.02 N.m, respectively. These values represent 44.21% and 15.91% of the average torque in the rated current, respectively. The optimized Bar-PM model has a peak-to-peak cogging torque value of 0.266 N.m, which is only 3.94% of the average torque in the rated current.

Equation 25 expresses the output torque ripple:

$$\%T_R = \frac{T_{max} - T_{min}}{T_{avg}} \times 100\% \quad (25)$$

where T_{avg} is the average torque, T_{min} is minimum torque, and T_{max} is the maximum torque, respectively. Using this technique, the reduction of cogging torque in an optimized Bar-PM motor is almost negligible. At a rated current density of 7.5 A/mm^2, the conventional ISTR, the proposed Bar-PM, and the optimized Bar-PM models exhibit average torque values of about 5.87, 6.41, and 6.74 N.m, respectively. In addition, these models have torque ripple values of 45.31%, 14.04%, and 4.15%, respectively.

Figure 11 demonstrates the output torque of DSAFFSPM models in the rated, the lower and the higher armature current for the rotor position. Comparing the average torques shows that the optimized Bar-PM model has higher average torque. Meanwhile, it has negligible torque ripple compared to the conventional ISTR.

Figure 12 depicts a relative operational index in rated ratio per each armature current density. It has defined as the torque average and percentage of torque ripple. It shows comparison of this index and illustrates that the optimized Bar-PM model has been located under the points. Thus, the optimized Bar-PM motor is designed for the best operational condition.

5. MODEL COMPARISON

5. 1. Comparison of the Mass and Costs

The price of each material expressed in $ and the quantity of

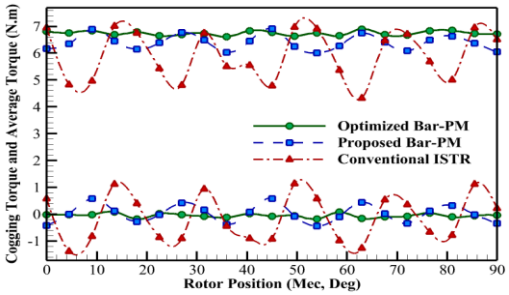

Figure 10. The cogging torque and output torque for the rotor mechanical position in three models

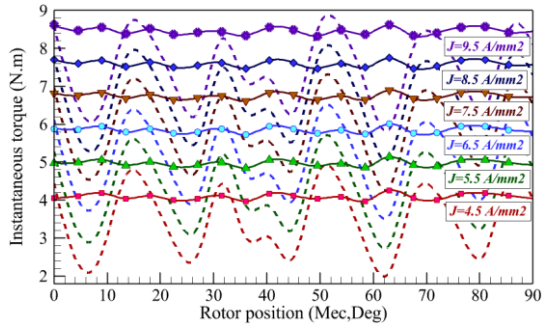

Figure 11. The output torque for the different armature currents as a function of the rotor position at @1500 rpm

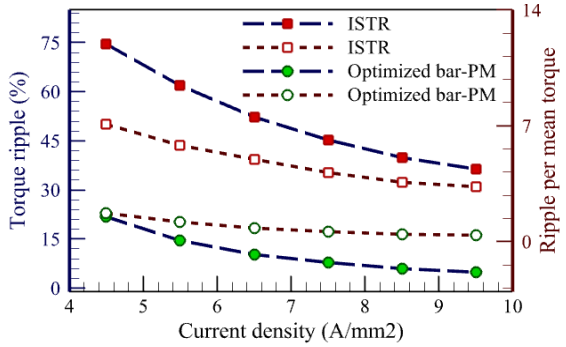

Figure 12. The torque ripple for the armature current density

materials utilized in kg are used to determine each machine's cost. Upon reviewing Table 3, it is clear that both the proposed and optimized Bar-PM models require significantly less PM material compared to the conventional ISTR models. Specifically, the proposed model uses 26.56% less while the optimized model uses 35.93% less. As a result, both models have a lower total cost, with the proposed model being up to 23.87% less expensive and the optimized model being up to 31.83% less expensive than the conventional ISTR models. To ensure a fair comparison, the consumables amount and cost of the optimized ISTR model were also optimized based on the optimized Bar-PM model.

TABLE 3. The mass and cost of the models

Model / Mass and Cost	ISTR [11]	Optimized ISTR [11]	Bar-PM	Optimized Bar-PM
Magnet weight [kg]	0.64	0.41	0.47	0.41
Steel weight [kg]	2.27	2.6	2.42	2.6
Copper weight [kg]	0.79	0.83	0.79	0.83
Total weight [kg]	3.7	3.84	3.68	3.84
Magnet price [$]	74.31	47.6	54.57	47.6
Steel price [$]	1.8	2.06	1.93	2.06
Copper price [$]	6.01	6.32	6.01	6.32
Total price [$]	82.12	55.98	62.51	55.98

5. 2. Comparison of the Performance Indices

The operational characteristics have been compared between the conventional ISTR, optimized ISTR, and the proposed and optimized Bar-PM models. The comparison results at 1500 rpm are listed in Table 4. The torque density of the optimized Bar-PM model is higher by as much as 14.88% and 5.04% compared to the conventional ISTR and proposed Bar-PM, respectively. While the torque density of the optimized ISTR model is lower by as much as 7.71% compared to the optimized Bar-PM model.

The optimized Bar-PM model, which has a torque-to-weight ratio of 1.75, has been enhanced by 9.71%, and 0.57% compared to the conventional ISTR and proposed model, respectively. Thus, the optimized model highlights the torque-to-cost ratio of 0.12 has been improved by as much as 69.01% and 17.64% compared to the conventional ISTR; and proposed Bar-PM, respectively. In the optimized Bar-PM model, the PM has been reduced by 35.93%, and the power-to-weight ratio of 0.089 has grown by 709.09% compared to the conventional ISTR model. Despite having a better torque-to-cost ratio than the ISTR and proposed bar-PM models, the optimized ISTR model still has issues with higher cogging torque and torque ripple. This affects the performance of the DSAFFSPM motor design, but the Bar-PM model has been developed to address these challenges.

Nonetheless, it has been revealed that the cogging torque value is 0.266 Nm, which is much lower compared to the conventional ISTR and proposed models, which are 90.08% and 75.23%, respectively. In addition, the torque ripple status for the optimized model is as much as 4.15% compared to conventional ISTR, and the proposed models decreased as much as 90.84%, and 70.44%, respectively. It has been declined that the cogging torque is as much as 90.32% compared to the optimized ISTR. While the torque ripple, it is suppression by as much as 89.79% compared to the optimized ISTR model. Machine efficiency is as follows:

$$\%\eta = \frac{T_{avg}\omega_r}{T_{avg}\omega_r + P_{cu} + P_{core}} \times 100\% \quad (26)$$

The losses are one of the main reasons for the low efficiency of the conventional ISTR model of much as 1.3% compared to the optimized model. in TABLE 4 represents the efficiency of the models as 92.96%, 93.48%, 94.13%, and 94.19%, respectively, regarding the efficient structure.

Comparing this section, it can be demonstrated that the proposed model with increased rotor pole pitch, and

TABLE 4. Performance indices comparison of the DSAFFSPM models

Parameter \ Model	ISTR [11]	Optimized ISTR [11]	Bar-PM	Optimized Bar-PM
Rated Speed [rpm]	1500			
Current Density [A/mm^2]	7.5			
Cogging torque [Nm]	2.52	2.75	1.02	0.266
Average torque [Nm]	5.87	6.22	6.41	6.74
Torque ripple [%]	45.31	40.67	14.04	4.15
Cogging torque/ Mean torque [%]	42.93	44.21	15.91	3.94
Power [kW]	0.922	0.976	1.006	1.058
Power density [kW/kg]	0.248	0.254	0.271	0.275
Power/Cost [kW/$]	0.011	0.0174	0.016	0.089
Torque density [Nm/L]	5.98	6.34	6.54	6.87
Torque/Total weight [Nm/kg]	1.58	1.61	1.74	1.75
Torque/ Total cost [Nm/$]	0.071	0.11	0.102	0.12
Torque/PM cost [Nm/$]	0.078	0.13	0.11	0.14
PM Weight [% of Total weight]	17.29	10.67	12.77	10.67
Total losses [W]	69.82	68.45	62.63	65.21
Efficiency [%]	92.96	93.48	94.13	94.19

reduced PM length technique had a superior performance in terms of high-torque density which was improved by 9.36% compared to that of the conventional. Although increasing the rotor pole pitch reduces flux concentration, but locating the PMs strategically generates higher torque with fewer PMs. To compensate, the rotor pole pitch width is slightly increased. While the conventional model has an overall cost of approximately $82.12, its proposed and optimized models reduce costs by 23.87% and 31.83% respectively. Therefore, it should be noted that the optimized model is with the lowest torque ripples and cogging torque. Although the target of this paper is on high-torque density and low-cost, suppression of the torque ripples and cogging torque are important objectives, as neglecting them can deteriorate the performance of the motor. Therefore, implementing the Bar-PM technique on the conventional ISTR of the optimized model can save rare-PM consumption and costs, in addition to improving performance. Finally, the proposed model satisfies approximately all the required objectives of EVs.

5. 3. The CPSR and Efficiency Map of the Model

The key parameters of designing AFFSBPM motors, high-torque density, high-efficiency, low-cost, torque ripple, and thermal stress are investigated in detail for EV applications. This section emphasizes the constant power speed range (CPSR), the losses, and the efficiency map. Considering the previous part, the three models are compared in the same condition; indices' results mean that the optimized Bar-PM model is highlighted because of the significant operational characteristics.

3D-FEM results of torque-versus-speed and power-versus-speed are plotted in Figure 13. The EV applications have required a reasonable CPSR of up to 3-4 times the base speed. Although the standard AFPM machine has as well as shorter CPSR of about 2 times the rated speed [23]. Using concentric-coils in the AFFSBPM design is extend the CPSR, so that a proper CPSR of about 3 times the rated speed is achieved. The optimized motor falls within the CPSR standard range due to its high output torque at speeds higher than the rated speed. In the optimized model, the iron loss and copper losses are raised by an increment of speed, and the total loss map is shown in Figure 14(a). However, it can be claimed that the efficiency has risen by an increment in the speed of a wide CPSR due to its approximately high-power density in Figure 14(b).

5. 4. Thermal Analysis The DSAFFSPM machines split active sources between two stators, resulting in

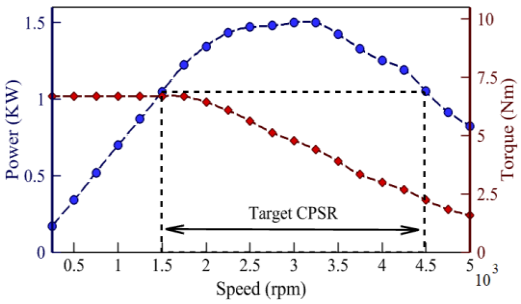

Figure 13. The torque and power curves vs. speeds

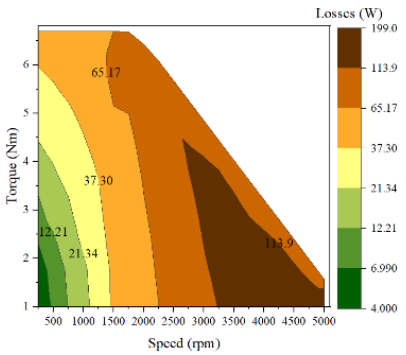

(a) The losses map

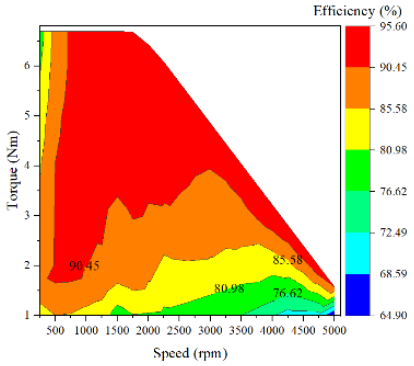

(b) The efficiency map

Figure 14. The efficiency map and torque-speed curves of the optimized Bar-PM model

lower temperatures than other PM machines. New design, with air channel between PMs, expected to perform better than conventional ISTR. The thermal analysis of the DSAFFSPM models under rated current and @1500 rotor speed is predicted by FEM. Figure 15 can be seen the temperature distribution in the DSAFFSPM models. In this condition, the calculated temperature decreases at the optimized Bar-PM compared with the conventional ISTR model. In the winding, high temperature has been caused by the high thermal conductivity of copper and the electric current which flows through the winding. The temperature of the winding in the optimized model is 56ºC, which is 15.15% lower than the conventional ISTR.

The maximum temperature of the stator for the optimized Bar-PM model is 55.94ºC, which decreased by 11.20% compared to conventional ISTR. The optimized Bar-PM model has the lowest inner/outer rotor temperature at 51.25ºC up to 47.14ºC, followed by the conventional ISTR at 60.93ºC up to 52ºC. Also, the temperature of the PM for the optimized Bar-PM model is 54.77ºC compared to conventional ISTR model, which decreased by as much as 13.69%, while the PM temperature in the inner part of the conventional ISTR model reached 66ºC.

The proposed motor topology is different from the conventional topology. In the flux-switching structure,

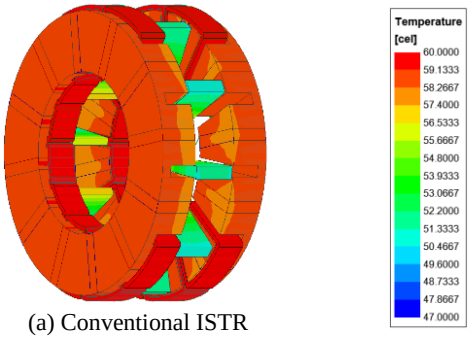

(a) Conventional ISTR

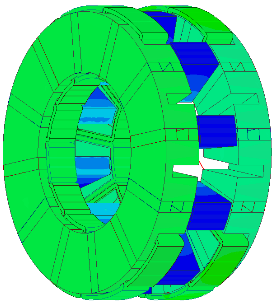

(b) Optimized Bar-PM

Figure 15. The thermal analysis in the DSAFFSPM models

all the active sources are in the stator. However, the proposed topology includes an air channel between the Bar-PMs and between the teeth of the segment-stator. This feature enables the temperature of the motor to be controlled and reduced by using the air channel.

6. CONCLUSION

This paper presents a technique that can be implemented on the PM of the motor with the aim of reducing the cost and increasing the torque density. The operational characteristics of the proposed motor have been improved through analytical design, sizing equations and multi-objective optimization. The main features of the motor are its high torque density and low cost due to the minimal use of PM in its structure. The cost coefficient for torque/PM is significantly higher in the optimized motor compared to the other one. The back EMF harmonic orders value for the optimized Bar-PM model is less than 2%. Therefore, the optimized model appears almost superior in the torque ripple and cogging torque indices. The proposed motor produces satisfactory power and torque densities and has flux-weakening capabilities for a CPSR up to 3 times the rated speed. The proposed model can be cost-effectively designed and successfully commercialized, making it suitable for use in EVs.

7. REFERENCES

1. Farrokh F, Vahedi A, Torkaman H, Banejad M, Faradonbeh VZ. A 2D hybrid analytical electromagnetic model of the dual-stator axial-field flux-switching permanent magnet motor. IET Electric Power Applications. 2024;18(2):252-64. 10.1049/elp2.12385
2. Nasiri-Zarandi R, Mohammadi Ajamloo A, Abbaszadeh K. Cogging torque minimization in transverse flux permanent magnet generators using two-step axial permanent magnet segmentation for direct drive wind turbine application. International Journal of Engineering, Transactions A: Basics. 2021;34(4):908-18. 10.5829/ije.2021.34.04a.17
3. Patel A, Suthar B. Cogging torque reduction of sandwiched stator axial flux permanent magnet brushless dc motor using magnet notching technique. International Journal of Engineering, Transactions A: Basics. 2019;32(7):940-6. 10.5829/ije.2019.32.07a.06

4. Ebrahimi H, Torkaman H, Javadi H. Simultaneous improvement of cogging torque and torque density in axial flux-switching permanent magnet motor. IET Electric Power Applications. 2023. 10.1049/elp2.12390
5. Patel A, Suthar B. Design optimization of axial flux surface mounted permanent magnet brushless dc motor for electrical vehicle based on genetic algorithm. International Journal of Engineering, Transactions A: Basics. 2018;31(7):1050-6. 10.5829/ije.2018.31.07a.07
6. Kazemain M, Ebrahimi-Nejad S, Jaafarian M. Experimental investigation of energy consumption and performance of reverse osmosis desalination using design of experiments method. International Journal of Engineering, Transactions A: Basics. 2018;31(1):79-87. 10.5829/ije.2018.31.01a.12
7. Mohammadi Ajamloo A, Ghaheri A, Shirzad H, Afjei E. Non-linear analytical modelling and optimisation of a 12/8 rotor excited flux-switching machine. IET Electric Power Applications. 2020;14(9):1592-603. 10.1049/iet-epa.2019.0732
8. Farahzadi M, Abbaszadeh K, Mirnikjoo S. Electromagnetic-Thermal Analysis of a Hybrid-Excited Flux Switching Permanent Magnet Generator for Wind Turbine Application. IEEE Transactions on Energy Conversion. 2023. 10.1109/TEC.2023.3269038
9. Ghaheri A, Afjei E, Torkaman H. A novel axial air-gap transverse flux switching PM generator: Design, simulation and prototyping. IET Electric Power Applications. 2023;17(4):452-63. 10.1049/elp2.12277
10. Zarghani A, Torkaman H, Arbab N, Toulabi MS. Lumped parameter thermal network for thermal analysis of a rotor-excited axial flux switching machine with electromagnetic-thermal design. Measurement. 2022;193:110971. 10.1016/j.measurement.2022.110971
11. Zhao W, Lipo TA, Kwon B-I. A novel dual-rotor, axial field, fault-tolerant flux-switching permanent magnet machine with high-torque performance. IEEE Transactions on Magnetics. 2015;51(11):1-4. 10.1109/TMAG.2015.2445926
12. Torkaman H, Ghaheri A, Keyhani A. Design of rotor excited axial flux-switching permanent magnet machine. IEEE Transactions on Energy Conversion. 2018;33(3):1175-83. 10.1109/TEC.2018.2807804
13. Zhang W, Liang X, Lin M. Analysis and comparison of axial field flux-switching permanent magnet machines with three different stator cores. IEEE Transactions on Applied Superconductivity. 2016;26(7):1-6. 10.1109/TASC.2016.2595588
14. Kim JH, Li Y, Sarlioglu B. Novel six-slot four-pole axial flux-switching permanent magnet machine for electric vehicle. IEEE Transactions on Transportation Electrification. 2016;3(1):108-17. 10.1109/TTE.2016.2620169
15. Farrokh F, Vahedi A, Torkaman H, Banejad M. Design and comparison of dual-stator axial-field flux-switching permanent magnet motors for electric vehicle application. IET Electrical Systems in Transportation. 2023;13(2):e12074. 10.1049/els2.12074
16. Yıldırız E, Güleç M, Aydın M. An innovative dual-rotor axial-gap flux-switching permanent-magnet machine topology with hybrid excitation. IEEE Transactions on Magnetics. 2018;54(11):1-5. 10.1109/TMAG.2018.2848878
17. Zhao J, Quan X, Lin M. Model predictive torque control of a hybrid excited axial field flux-switching permanent magnet machine. IEEE Access. 2020;8:33703-12. 10.1109/ACCESS.2020.2973360
18. Zhang W, Liang X, Yu F. Fault-tolerant control of hybrid excitation axial field flux-switching permanent magnet machines. IEEE Transactions on Magnetics. 2018;54(11):1-5. 10.1109/TMAG.2018.2827948
19. Han J, Zhang Z. Design and optimization of a low-cost hybrid-pole rotor for spoke-type permanent magnet machine. IEEE Transactions on Magnetics. 2021;58(2):1-5. 10.1109/TMAG.2021.3090655
20. Ullah W, Khan F, Hussain S, Alturise F. Investigation of low-cost dual port co-rotating dual rotor field excited flux switching generator for low-power rooftop wind turbine integrated with multi-port DC micro grid. IET Renewable Power Generation. 2022;16(14):3108-18. 10.1049/rpg2.12561
21. Muhammad A, Khan F, Ullah B, Milyani AH, Azhari AA. Design and FEM analysis of high-power density C-core permanent magnet transverse flux generator with reduced PM volume. IET Renewable Power Generation. 2023;17(4):885-93. 10.1049/rpg2.12642
22. Lin M, Hao L, Li X, Zhao X, Zhu Z. A novel axial field flux-switching permanent magnet wind power generator. IEEE Transactions on Magnetics. 2011;47(10):4457-60. 10.1109/TMAG.2011.2157908
23. Capponi FG, De Donato G, Caricchi F. Recent advances in axial-flux permanent-magnet machine technology. IEEE Transactions on Industry Applications. 2012;48(6):2190-205. 10.1109/TIA.2012.2226854
24. Arehpanahi M, Kheiry E. A New Optimization of Segmented Interior Permanent Magnet Synchronous Motor Based on Increasing Flux Weakening Range and Output Torque (Research Note). International Journal of Engineering. 2020;33(6):1122-7. 10.5829/ije.2020.33.06c.09
25. Chen Y, Zhuang J, Ding Y, Li X. Optimal design and performance analysis of double stator multi-excitation flux-switching machine. IEEE Transactions on Applied Superconductivity. 2019;29(2):1-5. 10.1109/TASC.2019.2891899

Persian Abstract

چکیده

در این مقاله، یک موتور شار میدان محوری شار سوئیچینگ مغناطیس دائم دو استاتور (DSAFFSPM) برای بهبود چگالی گشتاور و هزینه دستگاه پیشنهاد شده است. در این ساختار، استاتور دوگانه ۱۲ قطبی در دو طرف یک روتور ۱۰ قطبی دندانه داخلی قرار گرفته است. دو استاتور میزبان آهنربای مغناطیس دائم (PM) نوع Bar-PM و سیم پیچ‌ها است. نکته جدید این مطالعه ارائه تکنیکی است که می‌تواند بر روی آهترباهای ساختار DSAFFSPM اجرا شود. در این راستا، طرح تحلیلی پیشنهادی با یک معادله اندازه ارائه شده است و از بهینه‌سازی چند–هدفه برای دستیابی به اندازه بهینه با روش الگوریتم ژنتیک چند هدفه (MOGA) استفاده شده است. ویژگی‌های الکترومغناطیسی ماشین با استفاده از روش المان محدود سه–بعدی (3D-FEM) به دست آمده و تجزیه و تحلیل می‌شوند. مطالعه تطبیقی برای اثبات برتری شاخص های عملکرد انجام شده است. ساختار پیشنهادی به دلیل ریپل گشتاور و گشتاور دندانه‌ای کم دارای چگالی توان بالا، ارتعاش و نویز کم‌تری می‌باشد. در همین حال، ساختار پیشنهادی تنش حرارتی کمتری به دلیل راندمان بالا و تلفات هسته کم دارد. در نتیجه، ساختار پیشنهادی چگالی گشتاور بالا و هزینه کم را ارائه می‌کند که به طور خاص برای کاربردهای خودروهای الکتریکی (EVs) طراحی شده است.